MATERIALS SCIENCE

Visible light-gated reconfigurable rotary actuation of electric nanomotors

Zexi Liang¹ and Donglei Fan^{1,2}*

Highly efficient and widely applicable working mechanisms that allow nanomaterials and devices to respond to external stimuli with controlled mechanical motions could make far-reaching impact to reconfigurable, adaptive, and robotic nanodevices. We report an innovative mechanism that allows multifold reconfiguration of mechanical rotation of semiconductor nanoentities in electric (*E*) fields by visible light stimulation. When illuminated by light in the visible-to-infrared regime, the rotation speed of semiconductor Si nanowires in *E*-fields can instantly increase, decrease, and even reverse the orientation, depending on the intensity of the applied light and the AC *E*-field frequency. This multifold rotational reconfiguration is highly efficient, instant, and facile. Switching between different modes can be simply controlled by the light intensity at an AC frequency. We carry out experiments, theoretical analysis, and simulations to understand the underlying principle, which can be attributed to the optically tunable polarization of Si nanowires in an aqueous suspension and an external *E*-field. Finally, leveraging this newly discovered effect, we successfully differentiate semiconductor and metallic nanoentities in a noncontact and nondestructive manner. This research could inspire a new class of reconfigurable nanoelectromechanical and nanorobotic devices for optical sensing, communication, molecule release, detection, nanoparticle separation, and microfluidic automation.

Copyright © 2018
The Authors, some rights reserved; exclusive licensee
American Association for the Advancement of Science. No claim to original U.S. Government Works. Distributed under a Creative
Commons Attribution
NonCommercial
License 4.0 (CC BY-NC).

INTRODUCTION

Changing the working scheme of nanodevices from static to dynamic, from passive to active, enabling intelligent and autonomous performances, could bring unprecedented impact to an array of applications in electronics, communication, sensing, therapy, and single-cell biology research (1-12). Mechanically active materials and structures, which change volume, shape, and mechanical motions in response to external stimuli, are essential for realizing intelligent and autonomous electronics and have received immense research interest (13-15). For instance, the widely used shape memory alloys that undergo controlled volume change in external physical fields are now key elements of actuators widely used in aerospace, automobile, and precision instrumentation (16). Miniaturized mechanical grippers, made of strategically fabricated multilayer thin films with tailorable interfacial stresses, can readily selffold to capture live cells and sample biological tissues when sensing the acidic environment near the cells (17). More recently, mimicking live microorganisms in nature, artificial micro/nanorobotic devices have been fabricated with functionality analogous to the behavior of natural organisms (18). The acoustic hologram technique assembles particles into reconfigurable arbitrary patterns in time-evolving acoustic fields (19). Many techniques rely on light for motion control. Azobenzene chemical groups form shapes reconfigurable with light-induced isomerization in both macroscopic and molecular scales. These polymers are applied to carry out complex tasks, such as the capture and release of DNA molecules (20). Self-electrophoresis, based on photochemistry, has been exploited to develop light-guided micromotors with intrinsic asymmetric structures or light-induced asymmetry (21). Transition of TiO2 microspheres from swarm-like aggregation to monodispersive suspension is observed on exposure to ultraviolet light (22). The redistribution of electric (E) fields in response to light patterns on photoconductive substrates can readily translocate nanoparticles, cells, or droplets by dielectrophoresis or electrowetting (23, 24). Plasmonic nanostructures make it possible to control light in a subwavelength scope. With uniquely designed metallic structures, torques can be induced by a laser that compels the rotation (25). Thus, these remarkable materials that respond to external stimuli with mechanical actuations are highly potential for many unprecedented applications. However, most of these materials to date only respond to stimuli in one manner, for example, linear translocation, bending, rotation, or aggregation, and only work in limited environments. Moreover, to obtain these materials, sophisticated design, synthesis, and functionalization are often required. To overcome these bottlenecks, it is highly desirable to investigate a completely new mechanism in activating nanomaterials with efficient, reversible, and multifold reconfigurabilities.

Here, by controlling light stimuli, we achieve multifold mechanical reconfigurability of nanomechanical devices, that is, rotary nanomotors, in an efficient, versatile, and potentially widely applicable manner. The investigation is based on exploitation of the underlying interactions of electrokinetics around semiconductor Si nanowires, optically controlled interfacial polarization of Si nanowires in an aqueous suspension and applied high-frequency E-fields. We realize reconfigurable mechanical rotation of nanowires, including acceleration, deceleration, stop, and reversal of orientation by controlling illumination of visible light. We understand the working mechanism of both theoretical modeling and numerical simulations. With this newly discovered optomechanical effect, we demonstrate efficient noncontact differentiation of mixed metallic (Au) and semiconductor (Si) nanowires. This work could open new opportunities in the identification and separation of nanoparticles and live entities. It also inspires innovative approaches to equip nanomaterials and devices with multifold light-controlled mechanical reconfigurability for the emerging nanorobotics.

RESULTS

Arrays of silicon nanowires (diameter, 100 nm and above) are fabricated by modified metal-assisted chemical etching (MACE) templated through nanosphere assemblies (26, 27). The process is shown in Fig. 1A and discussed in detail in Materials and Methods. Briefly, we assemble

¹Materials Science and Engineering Program, University of Texas at Austin, Austin, TX 78712, USA. ²Department of Mechanical Engineering, University of Texas at Austin, Austin, TX 78712, USA.

^{*}Corresponding author. Email: dfan@austin.utexas.edu

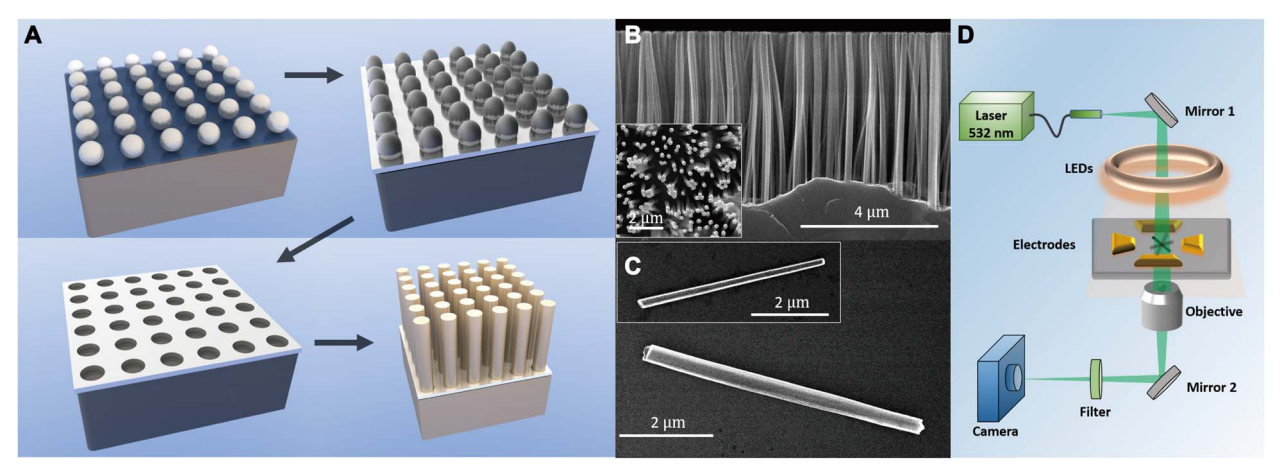


Fig. 1. Fabrication process of silicon nanowires and experimental setup. (A) Schematic of silicon nanowire fabrication via nanosphere lithography based on MACE. (B and C) SEM images of silicon nanowires. (B) Cross-sectional view of arrays of silicon nanowires of 200 nm in diameter made from n-type silicon wafers (560 to 840 ohm-cm) (inset: top view). (C) A nanowire of 500 nm in diameter (inset: a nanowire of 200 nm in diameter). (D) Schematic of the optical-electric setup for reconfigurable manipulation. LEDs, light-emitting diodes.

a monolayer of nanospheres on a silicon wafer as a mask for the deposition of Ag film. We then remove the nanospheres, leaving the Ag film with arrays of nanoholes. By immersing the sample in the etchant of hydrofluoric acid and hydrogen peroxide, we fabricate Si nanowires with controlled diameters, as shown in the scanning electron microscopy (SEM) images in Fig. 1 (B and C). For nanowires with diameters of less than 100 nm, we instead adopt one-step MACE (28). A droplet of nanowire suspension (20 μ l) is dispersed at the center of a quadruple microelectrode (500 μ m in gap) made of Au (100 nm)/Cr (5 nm) on glass. After allowing several minutes for the nanowires to deposit to the bottom, we record and analyze the motions. If not stated otherwise, the nanowires are 500 nm in diameter and 5 μ m in length, fabricated from n-type silicon wafers (560 to 840 ohm-cm).

We place the microelectrode on an inverted microscope equipped with a 532-nm laser as the stimulating source and a customized light-emitting diode ring with low illuminance (500 lux) as the background (Fig. 1D). By applying four AC voltages with a sequential 90° phase shift and at a frequency in the range of 2.5 kHz to 2 MHz on the quadruple electrodes, a rotating AC *E*-field can be readily created to rotate the nanowires, an effect termed as electrorotation. Figure 2A shows the distinct rotation characterizations with and without laser illumination versus AC frequencies from 5 kHz to 2 MHz at 20 Vpp (peak-to-peak voltage) (movie S1 to S4).

In the following, we name the blue and red curves with and without laser stimuli as the bright and dim spectra, respectively. The positive and negative signs of the rotation indicate the cofield and counterfield rotations of the nanowires to that of the external E-fields, respectively. The dim spectrum in Fig. 2A, obtained at low intensity of light (~500 lux), shows consistent cofield rotation in AC E-fields from 5 kHz to 2 MHz with a peak near 100 kHz. At low frequencies, for example, 2.5 kHz, some nanowires in suspension exhibit counterfield rotation. The differences from the rotation spectra reported previously (27) could be attributed to the differences in size, materials, and light conditions. However, under high-intensity illumination, we observe the reversal of the rotation orientation at frequencies of less than 50 kHz, as shown in the bright spectrum (red curve) in Fig. 2A. Besides the reversal of the rotation orientation, laser illumination substantially increases the absolute rotation speeds of the nanowires across the entire frequency region, except around the transition frequency at ~80 kHz. Two rotation peaks can be found at 10 and 750 kHz, corresponding to the maximum counterfield and cofield rotations, respectively. Overall, the effect of laser on the rotation spectra can be divided into four frequency regions: region I, low AC frequencies, below 5 kHz, increased rotation speed in the counterfield direction; region II, from 5 to 80 kHz, reversed rotation orientation from cofield to counterfield directions; region III, from 80 to 100 kHz, lowered rotation speed in the original cofield direction; region IV, from 100 kHz to 2 MHz, increased rotation speed in the original cofield direction.

After discovering the marked reconfigurable rotation of Si nanowires with optical illumination, we systematically investigated the effect of laser intensity on rotation spectra by tracking a single nanowire through all intensity conditions and frequencies (Fig. 2B). Obviously, the increase of the laser power from 0 to 255 mW cm⁻² enhances the rotation speed at both high and low frequencies, while the peak positions of the cofield rotation blue-shift from ~50 kHz to above 300 kHz monotonically.

We observe a similar optoresponsive rotation with laser illumination at 633 and 785 nm (127 mW cm⁻²), as shown in Fig. 3A. How the mechanical rotation of nanowires responds to light of different wavelengths is determined by their material properties as well as their geometries, which will be further investigated in a separation effort. Here, we found that the versatile reconfiguration of Si nanowires is widely attainable with a light source from the visible–to–near-infrared regime, which is desirable for a variety of applications.

We obtain the above strong light sensitivity in electrorotation from silicon nanowires of 500 nm in diameter. It is interesting to know whether such an optical reconfigurable effect can be obtained from nanowires of different dimensions. To investigate the size effect, we selected intrinsic Si nanowires to remove possible experimental uncertainties due to dopant variations if using n/p-type nanowires. We carry out a series of experiments. At a fixed diameter of 500 nm, we tested nanowires with four different lengths of 5, 7.5, 10, and 13 μm . The aforediscussed optoreconfigurable effect exists strongly in all of them, as shown in Fig. 3B. We found that light stimulation always blue-shifts the rotation spectra with significantly enhanced magnitude of peak speeds for both cofield and counterfield rotations. Furthermore, for conditions with or without light, with the increase of length of nanowires, the peak frequencies for cofield monotonically shift to lower frequencies. The

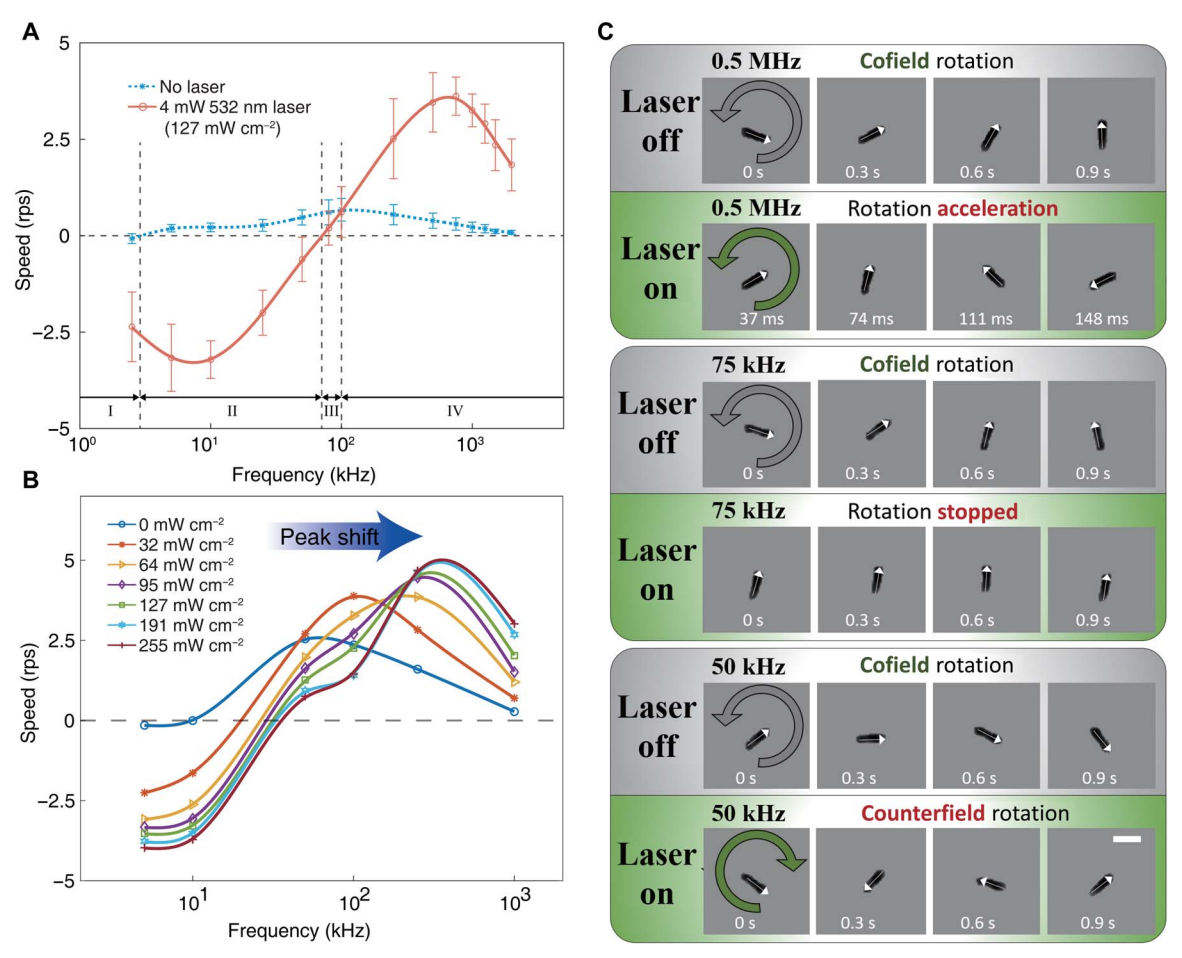


Fig. 2. Rotation of silicon nanowires and the reconfiguration by laser illuminance in *E*-fields. (A) Rotation speed versus AC frequency of silicon nanowires (n-type, 560 to 840 ohm-cm; length, 5 μm; diameter, 500 nm) in dim environment and under 532-nm laser illumination (127 mW cm⁻²). (B) Rotation versus AC frequency of silicon nanowires illuminated at different laser intensities (20 Vpp at all frequencies unless stated otherwise). We obtain the eye-guiding lines with cubic spline interpolation. (C) Snapshots of the rotation of single silicon nanowires in AC frequencies of 50 kHz to 0.5 MHz, showing three distinct optical responses. Scale bar, 5 μm.

peak magnitude also systematically decreases as the length of nanowires increases, which agrees with the modeling to be discussed later.

We also tested nanowires of different diameters of 500, 400 nm, and 200 nm with a same length of \sim 5 μ m, as shown in Fig. 3C. We also fabricate ultrafine nanowires with sub-100-nm diameters. All nanowires exhibit the optoreconfigurable responses, including the ultrafine wires of sub-100 nm in diameter. For larger-diameter nanowires of 400 to 500 nm, it can be found that the peak frequencies of cofield rotation are located fairly closely between 500 and 750 kHz. Such a peak frequency red-shifts to ~100 kHz when the diameter is decreased to 200 nm. We also observe that the magnitude of the peak speed of cofield rotation decreases with the reduced diameter of 200 nm. These results agree with the simulation to be discussed later. Here, we note that the peak frequencies of nanowires with 400- and 500-nm diameters are located closely with that of the 400-nm nanowires slightly positioned on the left. This can be attributed to the similar aspect ratios of 10 and 12.5 of these nanowires as well as the dimensional distribution from the fabrication process that can generate noticeable errors in the rotationspectrum tests. Although the movement of ultrafine nanowires due to Brownian motions is much stronger compared to other nanowires, we still observed the marked change of rotation speed when turning the laser on and off (Fig. 3D). With the 532-nm laser (127 mW cm⁻²),

the nanowire instantly switches to continuous rotation from random Brownian movement at an AC field of 0.5 MHz, as shown in the snapshots in Fig. 3E and movie S5. Overall, the experimental results of both the length and diameter dependence tests under laser illumination show expected and understandable trends.

These experimental studies demonstrate that the manner of reconfiguration of the nanowires, including acceleration, deceleration, and reversal of rotation chirality, depends on factors including AC frequency, laser power, and dimensions of silicon nanowires. The optical response of electrorotation is applicable to Si nanowires with a wide range of sizes and various resistivities from intrinsic (>5000 ohm · cm) to moderately n-doped silicon (0.6 to 0.75 ohm·cm), while the highly n-doped degenerate silicon nanowire (0.001 to 0.005 ohm·cm) does not respond to the light, which will be discussed later. The same effect is also observed in p-type silicon nanowires, as shown in Fig. S5, and can be applicable to other types of photosensitive semiconductors and polymers. To understand these complex phenomena, we conducted both theoretical analysis and numerical simulations.

Theoretical modeling and analysis

The rotational torques on small particles arise from the interactions of polarized particles and high-frequency rotating *E*-field (29). The electric

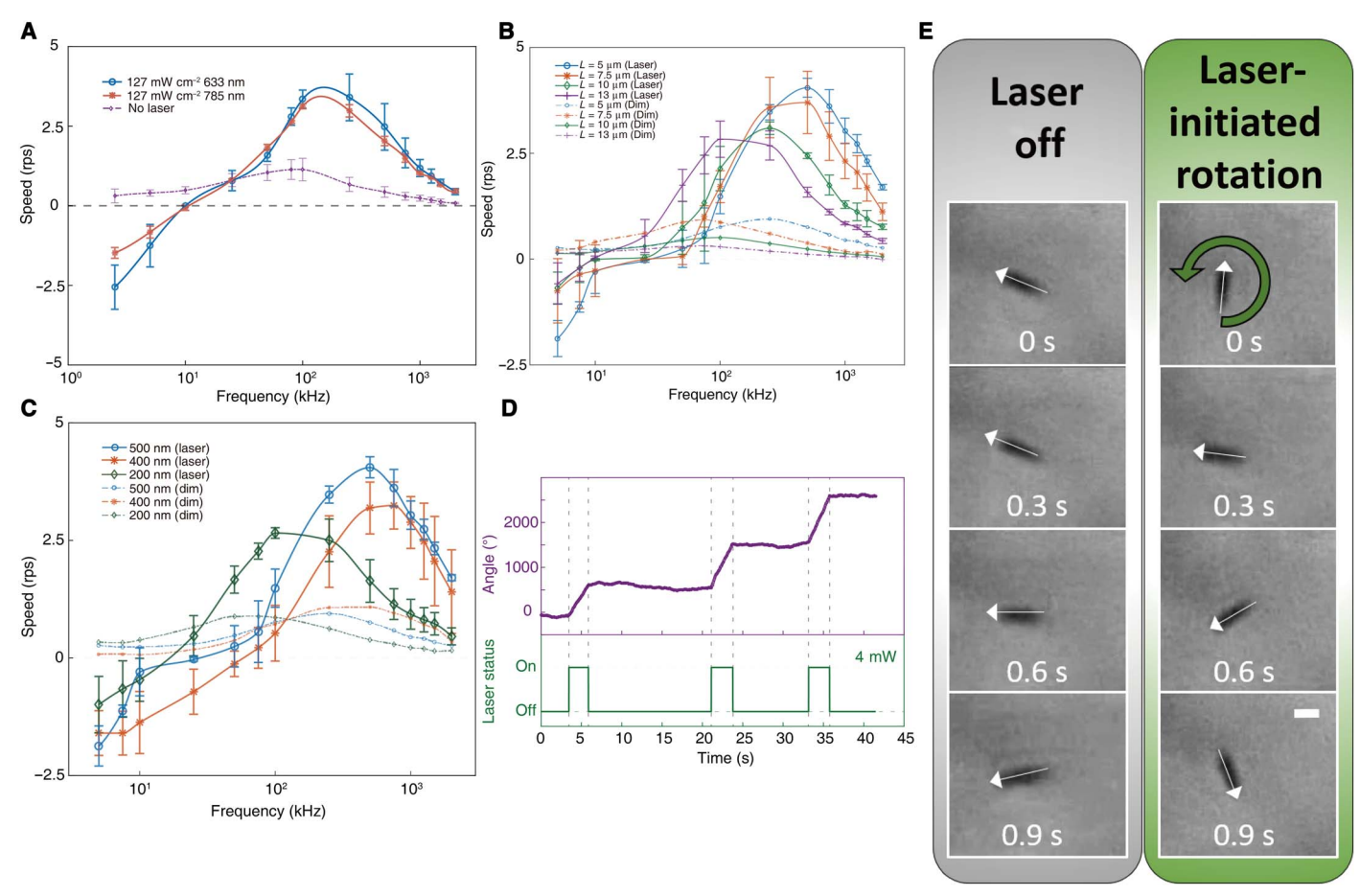


Fig. 3. Reconfigurable rotation of Si nanowires under different laser illumination and with different geometric dimensions in an AC *E*-field. (A) Rotation spectra of silicon nanowires under illumination of 633- and 785-nm lasers. (B) Rotation spectra of intrinsic silicon nanowires of 500 nm in diameter and lengths ranging from 5 to 13 μm. (C) Rotation spectra of intrinsic silicon nanowires of 5 μm in length and various diameters ranging from 200 to 500 nm. (D) Rotation angle versus time showing optically initiated rotation of nanowires of sub–100 nm in diameter (0.5 MHz and 20 Vpp). (E) Snapshots of laser-induced rotation of a nanowire of sub–100 nm in diameter. Scale bar, 2 μm. For a clearer view, the error bars of the dim spectra are shown in fig. S4 (B and E).

polarization of a nanoparticle is governed by multiple parameters including permittivity, conductivity and geometry of the nanoparticle and the electrical properties of suspension medium, as well as frequency of the rotating E-field. Theoretical models have been developed to understand the rotational behavior of metal and semiconductor nanowires. In addition to the long-established Maxwell-Wagner interfacial polarization effect (29), the electrical double layer (EDL) charging effect that also governs the rotation was identified recently (30, 31).

When a rotating AC *E*-field is applied via the quadruple electrodes, an electrical torque is exerted on the induced dipole moment of the nanowire and compels its rotation. Consider a nanowire placed in the center of a quadruple microelectrode with the long axis pointing along the *y* direction (Fig. 4A, top-down view). The nanowire is modeled as a long cylinder with a radius *r* and a length *L*. We generate a rotating AC *E*-feld by applying four AC voltages with 90° sequential phase shift on the quadruple electrodes. The *E*-field can be given by $\mathbf{E}(t) = E_0 \mathrm{Re}[(\hat{\mathbf{x}} - i\hat{\mathbf{y}})e^{i\omega t}]$ for the counterclockwise rotation. The nanowire is polarized with a total dipole moment (\mathbf{p}), expressed as $\mathbf{p} = \underline{\alpha}_x \mathbf{E}_x + \underline{\alpha}_y \mathbf{E}_y = \underline{\mathbf{p}}_x + \underline{\mathbf{p}}_y$, where $\underline{\alpha}_x$ and $\underline{\alpha}_y$ are the complex polarizability along the transverse and longitudinal axes of the nanowire, respectively. The underbars denote the complex variables with phasor. Since the angular frequency of the AC *E*-field is much higher than

that of the rotation speed of the nanowire, in the frequency region that we study, we can assume that the nanowire remains still while the AC *E*-field oscillating one cycle and then the time-averaged electrical torque can be readily written as

$$\mathbf{\tau}_{\mathrm{e}} = \frac{1}{2} \operatorname{Re} \left[\mathbf{\underline{p}}(t) \times \mathbf{\underline{E}}^{*}(t) \right] = -\frac{1}{2} E_{0}^{2} \operatorname{Im} \left[\alpha_{x} + \alpha_{y} \right] \hat{\mathbf{z}}$$
 (1)

Both the Maxwell-Wagner relaxation process and the effect of EDL contribute to the complex electric polarizability of the nanowire in an aqueous suspension. For a silicon nanowire suspended in deionized (DI) water in an *E*-field, charges accumulate at the interface between the two dielectrics due to the differences in electrical properties, including the permittivity and electrical conductivity. As the polarization involves several relaxation processes, the amount of charges accumulated at the interface depends on the AC frequencies, thus resulting in a frequency-dependent induced dipole moment, which is referred to as the Maxwell-Wagner polarization or relaxation. Meanwhile, once the interfacial polarization is established, the ions in suspension will be attracted toward the particle surface to screen the surface charge, which forms into an EDL. In general, we consider the polarization as a

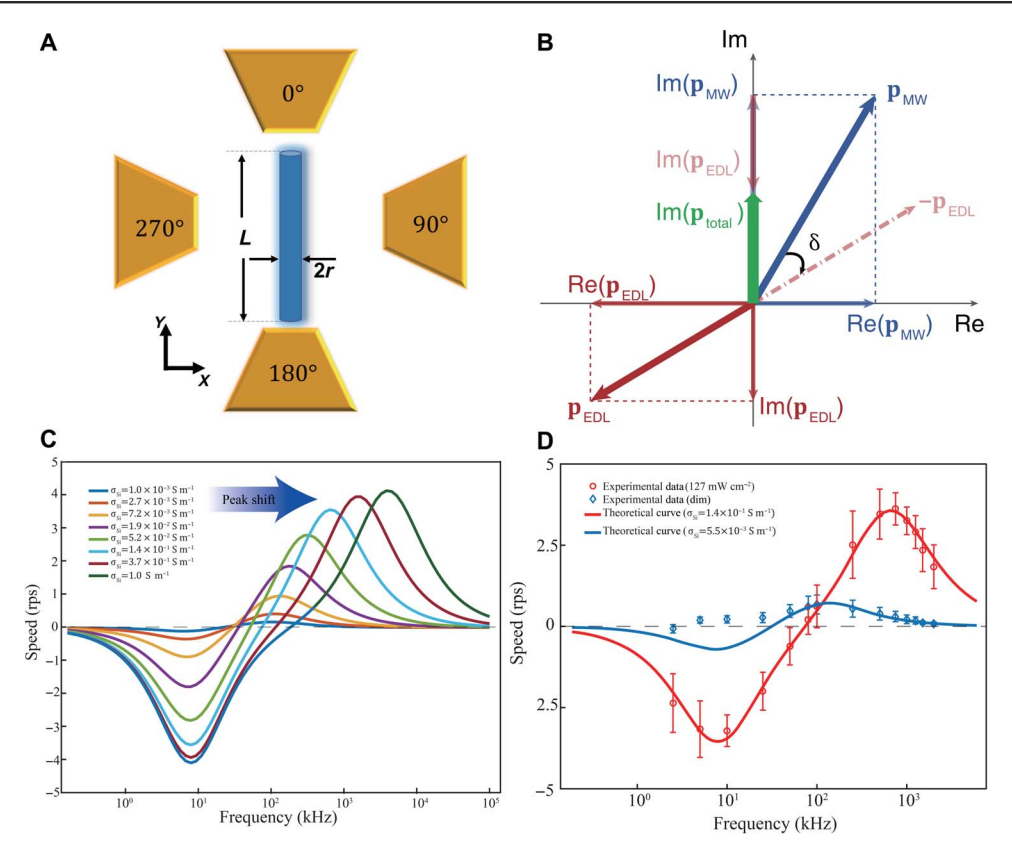


Fig. 4. Modeling of nanowire polarization and theoretical calculation of rotation speed versus AC frequency of silicon nanowires of $L = 5 \mu m$ and r = 250 nm. (A) Model of a silicon nanowire as a cylinder with length L and radius r. (B) Schematic of the real and imaginary dipole moment components induced by the Maxwell-Wagner relaxation and EDL effect. (C) Theoretical calculation of the rotation of nanowires of different electrical conductivities versus AC frequency. (D) Theory compared to the experimental results. We obtain the two particular electrical conductivities from fitting at the dim and bright conditions.

two-step process, in which the external *E*-field first induces the interfacial polarization and charges the surface, followed by the formation of EDL due to the surface charge attraction. Since the relaxation processes of both the Maxwell-Wagner polarization and EDL take finite time, there is a frequency-dependent phase lag between the Maxwell-Wagner polarization and the external *E*-field, as well as a frequency-dependent phase lag between the Maxwell-Wagner polarization and EDL under an AC *E*-field. Due to the synergistic effect, we obtain the rotation spectrum of Si nanowires, as shown in Fig. 4B.

We analytically carry out the modeling of the system. The Clausius-Mossotti factor (K_i) is the key term governing the Maxwell-Wagner polarizability along one of the principle axes (i) of a nanowire modeled as a prolate ellipsoid. We calculate it as

$$\underline{K_{i}} = \frac{\underline{\varepsilon_{p}} - \underline{\varepsilon_{m}}}{3(L_{i}(\underline{\varepsilon_{p}} - \underline{\varepsilon_{m}}) + \underline{\varepsilon_{m}})}$$
(2)

where $\underline{\varepsilon}_p$ and $\underline{\varepsilon}_m$ are the complex dielectric constants of the nanowire and the medium is defied as $\underline{\varepsilon}_j = \varepsilon_0 \varepsilon_{rj} - i \frac{\sigma_j}{\omega}$ (the subscript "j" is p or m, referring to the particle or medium), respectively; and L_i is the depolarization factor along one of the major axes $(a_y = L/2, a_x = a_z = r)$ given by

$$L_{i} = \frac{a_{x}a_{y}a_{z}}{2} \int_{0}^{\infty} \frac{ds}{(s+a_{i}^{2})B}$$
 (3)

where $B=\sqrt{(s+a_x^2)(s+a_y^2)(s+a_z^2)}$. Therefore, the overall in-plane dipole moment due to the Maxwell-Wagner relaxation $(p_{\rm MW})$ can be expressed as

$$\mathbf{p}_{\mathrm{MW}} = 4\pi a_{x} a_{y} a_{z} \varepsilon_{m} (\underline{K_{x} \mathbf{E}_{x}} + K_{y} \mathbf{E}_{y}) \tag{4}$$

We calculate both the real and imaginary parts of α_x and α_y . However, since the polarization of nanowire along the longitudinal y direction is much greater than that in the transverse x direction, one may approximate by only focusing on the dominating α_y .

Next, we analyzed how the EDL contributes to the imaginary part of the electric polarization in Eq. 1. We modeled the EDL by using an equivalent resistor-capacitor (RC) circuit with a time constant of τ_{RC} to understand the electrokinetic phenomena observed in our experiments. The EDL is formed because of the surface charge accumulation of the Maxwell-Wagner polarization, instead of direct response to the external E-field. While in a high-frequency AC field, the charging and discharging of the EDL cannot completely follow the Maxwell-Wagner polarization of the nanoparticle, which causes a phase lag. In a low-frequency limit, the charges due to the Maxwell-Wagner polarization on the nanowire can be fully screened by the EDL, resulting in $\mathbf{p}_{EDL} \approx -\mathbf{p}_{MW}$, where the total dipole moment essentially cancels out with a negligible negative residue ($0 < \frac{|\mathbf{p}_{EDL}| - |\mathbf{p}_{MW}|}{|\mathbf{p}_{MW}|} \ll 1$) as the thickness of EDL is much smaller compared to the size of the nanowire. In a high AC frequency, given the RC model, the resulted magnitude of dipole

moment of EDL can be expressed as $|\mathbf{p}_{\mathrm{EDL}}| = |\mathbf{p}_{\mathrm{MW}}| \frac{1}{\sqrt{\omega^2 \tau_{\mathrm{RC}}^2 + 1}}$. Here, we need to take phasor into consideration due to the phase lag between $-p_{\mathrm{EDL}}$ and p_{MW} , and we calculate the tangent of the phase lag (δ) as $\tan \delta = -\omega \tau_{\mathrm{RC}}$, the negative sign of which indicates a phase delay, as shown in Fig. 4B. Therefore, we calculate the imaginary part of EDL-induced dipole moment $\mathrm{Im}(\mathbf{p}_{\mathrm{EDL}})$ as

$$Im(\mathbf{p}_{EDL}) = -[Re(\mathbf{p}_{MW})\sin\delta + Im(\mathbf{p}_{MW})\cos\delta] \frac{1}{\sqrt{\omega^2 \tau_{RC}^2 + 1}}$$
 (5)

The total electric dipole moment of the nanowire system (p_{total}) includes both the Maxwell-Wagner relaxation process (p_{MW}) and the EDL component (p_{EDL}) . The imaginary component of p_{total} is given by

$$Im(\mathbf{p}_{total}) = Im(\mathbf{p}_{EDL}) + Im(\mathbf{p}_{MW})$$
 (6)

The values of different parameters used in the calculation are listed in table S1, in which τ_{RC} is chosen to best fit the experimental data of Fig. 2A. The electrical conductivity of Si is systematically swept from 1×10^{-3} S m⁻¹ to 1 S m⁻¹.

The nanowire suspended in water with a maximum rotation speed of less than 5 rps is within the low Reynolds number region (Re \ll 1), and thus, the system is in viscous laminar flow limit, free of turbulence with a constant drag coefficient of (32)

$$\gamma = \frac{\tau_{\eta}}{\omega} = \frac{\pi \eta l^3}{3(\sigma - 1.14 - 0.2\sigma^{-1} - 16\sigma^{-2} + 63\sigma^{-3} - 62\sigma^{-4})}$$
 (7)

where $\sigma=\ln\frac{L}{r}$. For a nanowire with 500-nm diameter and 5- μ m length, we calculate the drag coefficient as 8.3×10^{-20} N m s rad⁻¹. Therefore, the rotation spectrum of Si nanowires versus AC frequencies can be readily calculated theoretically by combining Eqs. 1 and 4 to 7, as shown in Fig. 4C.

It is known that, for semiconductors, photon excitation can generate additional free charge carriers, resulting in additional electrical conductivity, the so-called photoconductivity. Previous studies show that Si nanowires have strong photon response (33, 34), where the increase of electrical conductivity can reach several orders of magnitude. When we monotonically increase the electrical conductivity of Si from $1 \times$ 10⁻³ S m⁻¹ to 1 S m⁻¹, the peaks of both the cofield and counterfield rotations blue-shift, and the magnitudes of both increase substantially (Fig. 4C). These spectrum characteristics obtained from the calculation agree reasonably well with those obtained in our experiments, as shown in Fig. 4D. It suggests that the enhanced electrical conductivity of Si due to light illumination is the key factor that leads to the observed reconfigurability of rotation of nanowires. The theoretical fitting of the bright spectrum agrees well through the entire frequency range for an electrical conductivity of 1.4×10^{-1} S m⁻¹. Here, we noticed that this conductivity is close to that of the wafer from which the nanowires are synthesized. However, as shown by previous works, because of the surface depletion effects, the carrier density of Si nanowires is usually much lower than that of the wafer, since surface states at the interface between silicon and natural oxidization layer trap most carriers from dopants (note S2) (35, 36). With numerical simulation and calculation with consideration of light absorption and recombination rate, we further estimated the photoconductivity of Si nanowires (37–39), which is on the same order of magnitude of that obtained from the fitting. It suggests the good feasibility of the modeling. It also indicates that the photon-generated carriers contribute majorly to the effective conductivity of silicon at our light illumination conditions (note S3).

The theoretical fitting to dim spectrum agrees in high frequencies and deviates in low frequencies; for example, the counterfield rotation is shown in fitting but not observed in these experiments (Fig. 4D). This could be attributed to the simplified consideration of the charge distribution in nanowires that induce EDL when light is weak (dim environment). In reality, when light is dim, the carrier density is low, and the Maxwell-Wagner polarization–induced net charges not only accumulate at the surface but also distribute inside the silicon nanowire. Since the EDL is only sensitive to the surface charge, ineffective in responding to charges away from the surface, a weaker EDL compared to that used in the theoretical analysis is expected, which could account for the observed difference between the calculation and experiments at low frequencies.

We observe similar reconfigurable behaviors in a wide range of silicon nanowires made from n-doped wafers of 0.6 to 0.75 ohm-cm to intrinsic Si wafers of more than 5000 ohm·cm (fig. S1). For the Si nanowires made from Si wafers of 0.001 to 0.005 ohm·cm with a high doping level of ~ 10¹⁹ cm⁻³, the optical stimuli can no longer change the rotation behaviors (fig. S1). It can be attributed to the ultrahigh dopant concentration of 1×10^{19} cm⁻³ of the Si wafer, which corresponds to a carrier concentration six orders of magnitude higher than that induced by the laser excitation $(1.8 \times 10^{13} \text{ cm}^{-3})$, as shown in the calculation in note S3. The results further agree with our understanding that the increase of carrier density from photoexcitation leads to the responsiveness of the mechanical rotation of nanowires. Overall, the balance between the generation of photoexcited carriers and recombination, as well as the surface depletion effect, explains the observation of the general similarity of rotation spectra of nanowires made from silicon wafers with resistivity from 0.6 to more than 5000 ohm·cm, as well as the vanishing of the optical response in highly doped silicon nanowires with a resistivity of 0.001 to 0.005 ohm·cm.

By using the above modeling, we can also understand the dependence of electrorotation spectrum on lengths and diameters of nanowires with laser exposure, as previously shown in Fig. 3 (B and C). Here, we adopt the same diameters and lengths of nanowires in experiments in the modeling. The electrical conductivity of nanowires under laser exposure is set as 0.14 S m⁻¹ for all lengths, which is obtained from the above fitting. Here, we can consider that the photoconductivity of a nanowire is independent on the length of a nanowire when it is much longer than the wavelength of the laser. In our experiments, the shortest nanowire is 5 µm in length, around 10 times of the excitation light wavelength. Only high-order optical coupling modes exist along these nanowires, which has negligible influence on the light absorption. For nanowires with a fixed diameter of 500 nm and varied lengths from 5 to 15 μm, we simulate the electrorotation spectra, as shown in fig. S4C. The results show the monotonic redshift of the peak frequency of cofield rotation with the increase of the length of a nanowire, accompanied with the attenuation of the magnitudes of the peak speeds in both directions, which agrees well with the dependence observed in the experiments in Fig. 3B.

The modeling of the diameter dependence is more complex, since the absorption cross section of nanowires exposed to 532-nm laser depends on the diameter in the range of 100 to 500 nm. It results in varying photoconductivities among nanowires with different diameters, as shown in table S2. Note S4 includes detailed discussion. With the consideration of the varying photoconductivity, we can obtain the diameter-dependent simulation, as shown in fig. S4F. It shows a general trend that the peak frequency of cofield rotation red-shifts, and the magnitude of peak speed decreases with the reduction of the diameter of a nanowire, which is similar to that observed experimentally in Fig. 3C. Considering simulation and experimental results of both the length and diameter dependence, we can find that the aspect ratio of a nanowire plays the key role. Generally, the higher the aspect ratio, the lower the peak frequency and the magnitude of peak speed.

In the above analysis, we carefully omitted the light-induced heating effect around the Si nanowires, since the change of temperature under a laser of 127 mW cm⁻² is less than 10⁻⁴ K over 100 s, as shown by the numerical simulation by COMSOL (fig. S3). Thus, it is reasonable to neglect both temperature and viscosity changes in the experiments. Furthermore, it is interesting to note that, besides the feasible application in DI water, the optoreconfigurable effect of nanowires can be applied in low-concentration ionic solutions, for example, 1 to 10 parts per million of NaCl solutions, as shown in fig. S6. The optical

stimulation can greatly increase the manipulation efficiency and reconfigure nanowires on demand when in these ionic mediums compared to those without light. Note S5 includes the details.

Dynamic reconfigurable rotation of Si nanowires gated by white light

Silicon has a broadband absorption in the visible light region. Although all the aforementioned reconfigurable rotations of Si nanowires are demonstrated by monochromatic lasers from 532 to 785 nm, it may not be necessary to use lasers to induce the desired optoreconfigurable rotation of Si nanowires. Here, we tested the application of white light generated by a computer-controlled commercial projector to dynamically reconfigure the rotation of Si nanowires.

We customized an inverted optical microscope by equipping it with a commercial light projector (BenQ MW519) as the light source and a 6.5-mm fisheye lens (Opteka) placed above the microelectrodes for light focusing, as shown in Fig. 5A. We place the microelectrodes in the focal plane of the fisheye lens. We operate the commercial projector with a digital light processing system with 1280×720 pixel in resolution. We

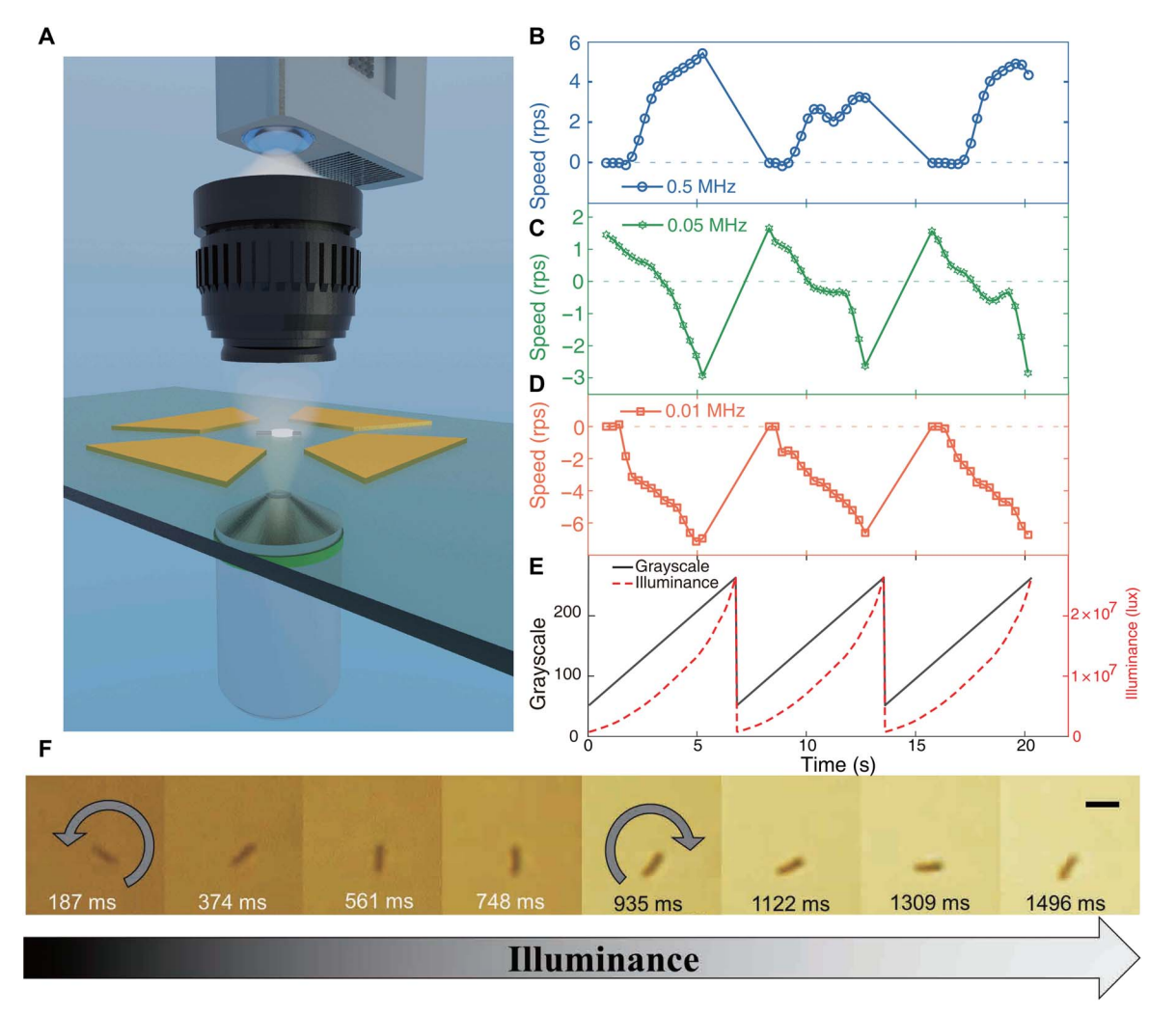


Fig. 5. Computer-programmable white light for reconfiguration of the silicon nanowire rotation. (A) Schematic of the white light projection system. (B to E) Rotation speed of nanowires versus light illuminance at three different AC frequencies. (B) Acceleration in both cofield and (D) counterfield rotations, (C) reversal of rotation. (E) Illuminance as a function of pixel grayscale value set to the projector. (F) Snapshots of rotation reversal with increase of illuminance (green curve in c, 0.05 MHz, 20 Vpp). Scale bar, 5 μm.

can readily design and project any colors and patterns of light to the nanowires with a resolution of $2 \, \mu m \times 2 \, \mu m$ per pixel. Here, we simply project a uniform monochromic rectangle, covering the entire central area of the microelectrodes and use a grayscale value from 0 to 255 to adjust the illuminance, where 0 refers to a completely dark image and 255 refers to the maximum illuminance.

We increased the grayscale value of the projected image from 50 to 255 at a constant rate of 30 grayscale values/s, repeated, and recorded the rotation behaviors of Si nanowires simultaneously. The illuminance as a function of grayscale value is nonlinear and shown in Fig. 5E. We apply three different rotating AC fields at 0.5, 0.05, and 0.01 MHz. We observed all four types of reconfigurations of rotation of Si nanowires, including acceleration, deceleration, and reversal of chirality of cofield rotation, and acceleration of counterfield rotation, as shown in Fig. 5 (B to D). We obtain the rotation speed versus the grayscale value (illuminance) of the light pattern repeated for three cycles at each AC frequency. At 0.5 MHz, the speed of the cofield rotation gradually increases with the grayscale value (illuminance) (Fig. 5B and movie S12). At 0.05 MHz, the nanowire begins with a cofield rotation in dark (grayscale value, 50), decreases to zero in speed, and then reverses the rotation direction when the grayscale value (illuminance) further increases (Fig. 5, C and F, and movie S11). At 0.01 MHz, the nanowire begins with a counterfield rotation in dark (grayscale value, 50) and increases in speed with the increase of grayscale value (illuminance) (Fig. 5D and movie S10). We instantly repeat all types of reconfigurable rotations by cycling the projected light patterns. Thus, plain white light can be used to dynamically reconfigure rotation of Si nanowires.

Distinguishing metal and semiconductor nanowires in a mixture

Finally, we applied this innovative optoreconfiguration technique to distinguish metallic and semiconductor nanowires in a noncontact and nondestructive manner. Our experiments and analysis discussed

above show that the optical reconfigurable rotation of semiconductor Si nanowires originates from the photoconductive effect in semiconductors. While, for metallic nanoparticles, with much higher density of electrons compared to that in semiconductors, the illumination cannot change their electrical conductivity. With this understanding, we demonstrated the application in distinguishing metallic and semiconductor nanowires by a plain optical stimulation in a rotating E-field. For a proof of concept, we mixed intrinsic silicon nanowires with gold nanowires in the same suspension in the test. It is difficult to distinguish the metallic and semiconductor nanowires with bright-field optical microscopic imaging. However, when we subject the nanowires to 5 kHz rotating AC fields and periodic illumination of 532-nm laser at 32 mW cm⁻², we find distinct behaviors for metallic and semiconductor nanowires. The semiconductor Si nanowires show periodic changes in rotation synchronized with the laser illuminance, and metallic nanowires rotate at constant speeds with no response to the laser, as shown in Fig. 6 (A and B) (movie S13). For silicon nanowires, various optical responses can be observed including acceleration, deceleration, reversal rotation, and stopping, depending on the geometries and electrical properties. Although the reconfigurations of the Si nanowires can be different, and some are hard to distinguish from fluctuations caused by Brownian motion, after taking Fourier analysis of the plot of angle versus time, it is straightforward to identify silicon nanowires by the existence of a peak at the illumination frequency $(^{1}/_{6}$ Hz in Fig. 6D), while the spectrum for gold nanowire is flat through all frequencies with no obvious peaks. In this way, we can readily determine the semiconductor Si nanowires and metallic Au nanowires in the same suspension with high accuracy. On the basis of this working principle and with further technical development, identification of materials with less distinction could be achieved. For instance, semiconductor nanomaterials with different band gaps and absorption spectra could be distinguished by observing and analyzing their rotation behaviors in E-fields under light stimuli of a series of wavelengths.

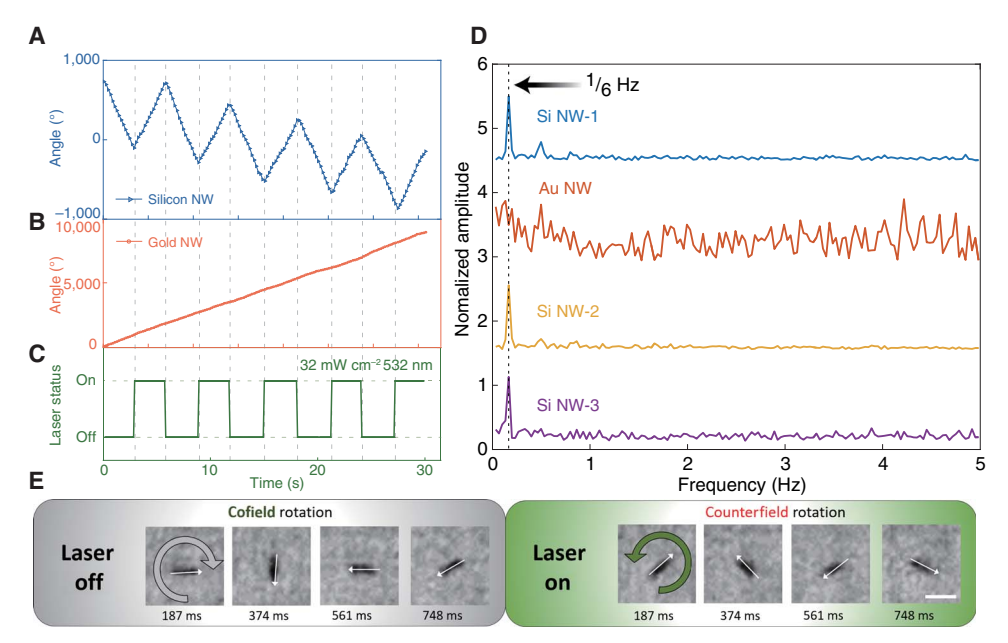


Fig. 6. Different responses in rotation of semiconductor and metallic nanowire under laser stimuli in *E*-fields. Angle versus time of (**A**) silicon and (**B**) gold nanowires (NWs). (**C**) Laser of 532 nm (32 mW cm⁻²) is on and off periodically. (**D**) Fourier analysis of rotation angle increment per frame. All amplitudes are normalized. The peaks at $^{1}/_{6}$ Hz, same as that of the periodic laser stimuli, are only found in silicon nanowires. (**E**) Snapshots of a silicon nanowire: distinct rotating behavior when laser is on or off. Scale bar, 5 μm.

DISCUSSION

Here, we discovered a new working mechanism that can readily reconfigure mechanical motions of semiconductor nanowires including acceleration, deceleration, stopping, and reversal of rotation merely by controlling the external light intensity in an E-field. This finding can be considered as a mechanical analogy of field-effect transistors gated by light. We understood the working mechanism with both theoretical analysis and numerical simulations and successfully demonstrated its application in distinguishing semiconductor from metal nanowires in the same suspension. With this discovery, potentially, various nanoentities, devices, and even biological cells could be equipped with mechanical responsiveness and multifold reconfigurability with functionalized semiconductor elements, changing their motion paradigms from passive to dynamic. Individually controlled micro/nanomachines amidst many could be achievable, which couple and reconfigure their operations instantly. This research could open up many opportunities for interdisciplinary fields, including reconfigurable optical devices, nanoelectromechanical system, nanorobots, nanomachines, communication, tunable molecule release, nanoparticle separation, and microfluidic automation.

MATERIALS AND METHODS

Fabrication of silicon nanowires

The silicon nanowires used in this work were fabricated via two similar methods depending on the diameter. For nanowires with a diameter of greater than 100 nm, nanosphere lithography masked MACE was used (26). First, all silicon wafers of various doping density from intrinsic (>5000 ohm·cm) to highly doped (0.001 to 0.005 ohm·cm) were rinsed and sonicated in acetone, isopropanol (IPA), and DI water each for 5 min sequentially. After drying in nitrogen gas flow, the wafers were immersed in poly(diallyldimethylammonium chloride) [2 weight % (wt %)], poly(sodium 4-styrenesulfonate) (2 wt %), and aluminum chlorohydrate (5 wt %) each for 30 s that the surface can be modified with positive/negative/positive charge layers. Next, after immersing the wafer into a polystyrene (PS) sphere suspension for 2 min, a monodispersed layer of negatively charged PS nanospheres was formed on the wafer. Subsequently, a reactive ion etching process was carried out to slightly reduce the size of PS spheres and to remove the charged polyelectrolyte layers. Then, a thin silver film of 50 nm in thickness was deposited on the wafer by electron-beam evaporation. Next, we sonicated the wafer in toluene to remove the PS spheres, leaving arrays of nanoholes on the silver film. The etching was conducted in the mixture of 4.7 M HF and 0.3 M H₂O₂. Finally, silver was removed by nitric acid, and nanowires were sonicated off the wafer in DI water. For nanowires with a diameter of less than 100 nm, one step synthesis was adopted by directly immersing the cleaned wafer into the mixture of 4.7 M HF and 0.02 M AgNO₃ (28). After the etching, we treated the wafer with nitric acid to remove the silver dendrite and then sonicated nanowires off the wafer in DI water.

Fabrication of quadruple electrodes

A glass slide was cleaned by sonication for 3 min sequentially in acetone, IPA, and DI water. Then, 5-nm Cr and 100-nm Au films were deposited onto the glass substrate via electron-beam evaporation. We made a quadruple microelectrode on the glass slide with a standard photolithography process by using S1811 photoresist, designed photomasks, and commercially available Au/Cr etchant. The microelectrode was obtained after the removal of the photoresist with acetone. The

microelectrodes were connected to external electronics by silver pasteattached wires.

Optical setup

We used an Olympus IX70 inverted microscope to carry out the experiments. We customized a ring-shipped LED light source to provide the background illumination and to allow the laser to pass through and equipped it on the microscope. A 532-nm sapphire laser made by Coherent was used as the laser source. The LED illuminance was measured by Dr. Meter LX1330B. Laser power was measured by a Newport 1917-R power meter. We used a BenQ MW519 projector for the dynamic light projection and an Opteka 6.5-mm fisheye lens to focus the light pattern onto the quadruple microelectrodes.

Electrical circuit

Two Agilent 33250A function generators were used as the signal sources. The signals were processed into four with sequential 90° phase shift by a customized circuit board with LM6181IN Op Amps (Texas Instruments).

SUPPLEMENTARY MATERIALS

Supplementary material for this article is available at http://advances.sciencemag.org/cgi/content/full/4/9/eaau0981/DC1

Table S1. Values of parameters of Si nanowire and medium used in the modeling.

Table S2. Optical and electrical properties of nanowires with different diameters obtained by simulation and calculation.

Note S1. Instant light responsiveness.

Note S2. Surface depletion effects in silicon nanowires.

Note S3. Light absorption and photoconductivity.

Note S4. Modeling the dependence of rotation spectrum on diameters of nanowires.

Note S5. Compatibility of the light modulation of nanowire rotation in ionic solution.

Fig. S1. Rotation spectra of nanowires made from silicon wafers of various n-doping densities. Fig. S2. Light absorption of silicon nanowires.

Fig. S3. Temperature profile around a Si nanowire in water after 100-s exposure to 532-nm laser (127 mW cm $^{-2}$).

Fig. S4. Experimental and modeling results of rotation spectra of nanowires with different dimensions in an AC *E*-field.

Fig. S5. Experimental result of the bright and dim rotation spectra of nanowires with 500 nm in diameter and 5 μ m in length, made from p-type silicon wafer (0.1 to 0.6 ohm-cm).

Fig. S6. Experimental and simulation results of the bright and dim rotation spectra of intrinsic silicon nanowire (r = 500 nm; $L = 5 \mu m$) in solutions with various ionic strengths.

Movie S1. The silicon nanowire is made from n-doped silicon wafer (560 to 840 ohm-cm) and suspended in DI water.

Movie S2. Counterfield rotation acceleration under 2.5 kHz, 20 Vpp $\it E$ -field, and 532-nm laser (127 mW cm $^{-2}$).

Movie S3. Cofield to counterfield reversal under 50 kHz, 20 Vpp $\it E$ -field, and 532-nm laser (127 mW cm $^{-2}$).

Movie S4. Cofield acceleration under 0.5 MHz, 20 Vpp E-field, and 532-nm laser (127 mW cm $^{-2}$). Movie S5. Laser-initiated rotation of a nanowire with sub-100-nm diameter under 0.5 MHz, 20 Vpp E-field, and 532-nm laser (127 mW cm $^{-2}$).

Movie S6. Rotation reversal of multiple nanowires under 25 kHz, 20 Vpp E-field, 532-nm laser (127 mW cm $^{-2}$), and 0.5× play speed.

Movie S7. Multiple nanowires change from rotation to still under 100 kHz, 20 Vpp $\it E$ -field, 532-nm laser (127 mW cm $^{-2}$), and 0.5× play speed.

Movie S8. Cofield rotation acceleration of multiple nanowires under 0.5 MHz, 20 Vpp E-field, 532-nm laser (127 mW cm $^{-2}$), and 0.5× play speed.

Movie S9. Multiple nanowires change from still to rotation under 2 MHz, 20 Vpp E-field, 532-nm laser (127 mW cm $^{-2}$), and 0.5× play speed.

Movie S10. Dynamic rotation control of counterfield rotation acceleration by white light digital light processing under 10 kHz and 20 Vpp *E*-field.

Movie S11. Dynamic control of rotation reversal by white light digital light processing under 50 kHz and 20 Vpp E-field.

Movie S12. Dynamic control of cofield rotation acceleration by white light digital light processing under 0.5 MHz and 20 Vpp *E*-field.

Movie S13. Rotation of silicon and gold nanowires in a mixture under 5 kHz and stimulated by 532-nm a periodic laser (32 mW cm⁻²).

Reference (40)

REFERENCES AND NOTES

- R. K. Soong, G. D. Bachand, H. P. Neves, A. G. Olkhovets, H. G. Craighead,
 C. D. Montemagno, Powering an inorganic nanodevice with a biomolecular motor.

 Science 290. 1555–1558 (2000).
- A. M. Fennimore, T. D. Yuzvinsky, W.-Q. Han, M. S. Fuhrer, J. Cumings, A. Zettl, Rotational actuators based on carbon nanotubes. *Nature* 424, 408–410 (2003).
- W. F. Paxton, K. C. Kistler, C. C. Olmeda, A. Sen, S. K. St. Angelo, Y. Cao, T. E. Mallouk, P. E. Lammert, V. H. Crespi, Catalytic nanomotors: Autonomous movement of striped nanorods. J. Am. Chem. Soc. 126, 13424–13431 (2004).
- S. Fournier-Bidoz, A. C. Arsenault, I. Manners, G. A. Ozin, Synthetic self-propelled nanorotors. Chem. Commun. 441–443 (2005).
- J. Xi, J. J. Schmidt, C. D. Montemagno, Self-assembled microdevices driven by muscle. Nat. Mater. 4, 180–184 (2005).
- C. Cvetkovic, R. Raman, V. Chan, B. J. Williams, M. Tolish, P. Bajaj, M. Selman Sakar, H. Harry Asada, M. T. A. Saif, R. Bashir, Three-dimensionally printed biological machines powered by skeletal muscle. *Proc. Natl. Acad. Sci. U.S.A.* 111, 10125–10130 (2014).
- D. Fan, Z. Yin, R. Cheong, F. Q. Zhu, R. C. Cammarata, C. L. Chien, A. Levchenko, Subcellular-resolution delivery of a cytokine through precisely manipulated nanowires. Nat. Nanotechnol. 5, 545–551 (2010).
- W. Wang, S. Li, L. Mair, S. Ahmed, T. J. Huang, T. E. Mallouk, Acoustic propulsion of nanorod motors inside living cells. *Angew. Chem. Int. Ed. Engl.* 53, 3201–3204 (2014).
- J. X. Li, W. Liu, T. Li, I. Rozen, J. Zhao, B. Bahari, B. Kante, J. Wang, Swimming microrobot optical nanoscopy. *Nano Lett.* 16, 6604–6609 (2016).
- K. Kim, X. Xu, J. Guo, D. L. Fan, Ultrahigh-speed rotating nanoelectromechanical system devices assembled from nanoscale building blocks. *Nat. Commun.* 5, 3632 (2014).
- X. Xu, K. Kim, D. L. Fan, Tunable release of multiplex biochemicals by plasmonically active rotary nanomotors. *Angew. Chem. Int. Ed. Engl.* 54, 2525–2529 (2015).
- L. Zhang, T. Petit, Y. Lu, B. E. Kratochvil, K. E. Peyer, R. Pei, J. Lou, B. J. Nelson, Controlled propulsion and cargo transport of rotating nickel nanowires near a patterned solid surface. ACS Nano 4, 6228–6234 (2010).
- L. Liu, S. Jiang, Y. Sun, S. Agarwal, Giving direction to motion and surface with ultra-fast speed using oriented hydrogel fibers. Adv. Funct. Mater. 26, 1021–1027 (2016).
- X. Zhang, Z. Yu, C. Wang, D. Zarrouk, J.-W. T. Seo, J. C. Cheng, A. D. Buchan, K. Takei, Y. Zhao, J. W. Ager, J. Zhang, M. Hettick, M. C. Hersam, A. P. Pisano, R. S. Fearing, A. Javey, Photoactuators and motors based on carbon nanotubes with selective chirality distributions. *Nat. Commun.* 5, 2983 (2014).
- K. Han, C. Wyatt Shields IV, N. M. Diwakar, B. Bharti, G. P. López, O. D. Velev, Sequence-encoded colloidal origami and microbot assemblies from patchy magnetic cubes. Sci. Adv. 3, e1701108 (2017).
- J. M. Jani, M. Leary, A. Subic, M. A. Gibson, A review of shape memory alloy research, applications and opportunities. *Mater. Des.* 56, 1078–1113 (2014).
- T. G. Leong, C. L. Randall, B. R. Benson, N. Bassik, G. M. Stern, D. H. Gracias, Tetherless thermobiochemically actuated microgrippers. *Proc. Natl. Acad. Sci. U.S.A.* 106, 703–708 (2009).
- C. Chen, X. Chang, H. Teymourian, D. E. Ramírez-Herrera, B. Esteban-Fernández de Ávila, X. Lu, J. Li, S. He, C. Fang, Y. Liang, F. Mou, J. Guan, J. Wang, Bioinspired chemical communication between synthetic nanomotors. *Angew. Chem. Int. Ed. Engl.* 57, 241–245 (2018).
- 19. K. Melde, A. G. Mark, T. Qiu, P. Fischer, Holograms for acoustics. *Nature* **537**, 518–522 (2016).
- S. K. M. Nalluri, J. Voskuhl, J. B. Bultema, E. J. Boekema, B. J. Ravoo, Light-responsive capture and release of DNA in a ternary supramolecular complex. *Angew. Chem. Int. Ed.* 50, 9747–9751 (2011).
- L. Xu, F. Mou, H. Gong, M. Luo, J. Guan, Light-driven micro/nanomotors: From fundamentals to applications. Chem. Soc. Rev. 46, 6905–6926 (2017).
- Y. Hong, M. Diaz, U. M. Córdova-Figueroa, A. Sen, Light-driven titanium-dioxide-based reversible microfireworks and micromotor/micropump systems. *Adv. Funct. Mater.* 20, 1568–1576 (2010).
- P. Y. Chiou, A. T. Ohta, M. C. Wu, Massively parallel manipulation of single cells and microparticles using optical images. *Nature* 436, 370–372 (2005).

- S. Arscott, Moving liquids with light: Photoelectrowetting on semiconductors. Sci. Rep. 1, 184 (2011).
- L. Shao, Z.-J. Yang, D. Andrén, P. Johansson, M. Käll, Gold nanorod rotary motors driven by resonant light scattering. ACS Nano 9, 12542–12551 (2015).
- Z. Huang, H. Fang, J. Zhu, Fabrication of silicon nanowire arrays with controlled diameter, length, and density. Adv. Mater. 19, 744–748 (2007).
- X. Xu, C. Liu, K. Kim, D. L. Fan, Electric-driven rotation of silicon nanowires and silicon nanowire motors. Adv. Funct. Mater. 24, 4843–4850 (2014).
- K.-Q. Peng, Y.-J. Yan, S.-P. Gao, J. Zhu, Synthesis of large-area silicon nanowire arrays via self-assembling nanoelectrochemistry. Adv. Mater. 14, 1164–1167 (2002).
- 29. T. B. Jones, T. B. Jones, Electromechanics of Particles (Cambridge Univ. Press, 2005).
- J. J. Arcenegui, P. Garcia-Sánchez, H. Morgan, A. Ramos, Electro-orientation and electrorotation of metal nanowires. *Phys. Rev. E Stat. Nonlin. Soft Matter Phys.* 88, 063018 (2013)
- P. Garcia-Sánchez, A. Ramos, Electrorotation and electroorientation of semiconductor nanowires. *Langmuir* 33, 8553–8561 (2017).
- S. Broersma, Rotational diffusion constant of a cylindrical particle. J. Chem. Phys. 32, 1626–1631 (1960).
- A. Zhang, H. Kim, J. Cheng, Y.-H. Lo, Ultrahigh responsivity visible and infrared detection using silicon nanowire phototransistors. *Nano Lett.* 10, 2117–2120 (2010).
- S. L. Tan, X. Zhao, K. Chen, K. B. Crozier, Y. Dan, High-performance silicon nanowire bipolar phototransistors. Appl. Phys. Lett. 109, 033505 (2016).
- B. S. Simpkins, M. A. Mastro, C. R. Eddy Jr., P. E. Pehrsson, Surface depletion effects in semiconducting nanowires. J. Appl. Phys. 103, 104313 (2008).
- V. Schmidt, S. Senz, U. Gösele, Influence of the Si/SiO₂ interface on the charge carrier density of Si nanowires. Appl. Phys. A 86, 187–191 (2007).
- E. M. Grumstrup, M. M. Gabriel, E. M. Cating, C. W. Pinion, J. D. Christesen, J. R. Kirschbrown, E. L. Vallorz III, J. F. Cahoon, J. M. Papanikolas, Ultrafast carrier dynamics in individual silicon nanowires: Characterization of diameter-dependent carrier lifetime and surface recombination with pump–probe microscopy. J. Phys. Chem. C 118, 8634–8640 (2014).
- Y. Dan, K. Seo, K. Takei, J. H. Meza, A. Javey, K. B. Crozier, Dramatic reduction of surface recombination by in situ surface passivation of silicon nanowires. *Nano Lett.* 11, 2527–2532 (2011).
- O. Demichel, V. Calvo, A. Besson, P. Noé, B. Salem, N. Pauc, F. Oehler, P. Gentile, N. Magnea, Surface recombination velocity measurements of efficiently passivated gold-catalyzed silicon nanowires by a new optical method. *Nano Lett.* 10, 2323–2329 (2010).
- S. Kato, T. Yamazaki, Y. Kurokawa, S. Miyajima, M. Konagai, Influence of fabrication processes and annealing treatment on the minority carrier lifetime of silicon nanowire films. *Nanoscale Res. Lett.* 12, 242 (2017).

Acknowledgments: We thank C. Liu, K. Kim, J. Guo, Z. Wang, and D. Teal for the helpful technical support and discussions. Funding: We are grateful for the support of NSF via the CAREER Award (grant no. CMMI 1150767) and research grant EECS-1710922 and Welch Foundation (grant no. F-1734). Author contributions: D.F. conceived and supervised the project. Z.L. performed experiments, conceived, and carried out modeling. Both authors analyzed and discussed the results and co-wrote the manuscript. Competing interests: The authors plan to file a U.S. patent and declare that they have no other competing interests. Data and materials availability: All data needed to evaluate the conclusions in the paper are present in the paper and/or the Supplementary Materials. Additional data related to this paper may be requested from the authors.

Submitted 6 May 2018 Accepted 31 July 2018 Published 14 September 2018 10.1126/sciadv.aau0981

Citation: Z. Liang, D. Fan, Visible light-gated reconfigurable rotary actuation of electric nanomotors. *Sci. Adv.* 4, eaau0981 (2018).



Visible light-gated reconfigurable rotary actuation of electric nanomotors

Zexi Liang and Donglei Fan

Sci Adv 4 (9), eaau0981. DOI: 10.1126/sciadv.aau0981

ARTICLE TOOLS http://advances.sciencemag.org/content/4/9/eaau0981

SUPPLEMENTARY MATERIALS http://advances.sciencemag.org/content/suppl/2018/09/10/4.9.eaau0981.DC1

REFERENCES This article cites 38 articles, 4 of which you can access for free http://advances.sciencemag.org/content/4/9/eaau0981#BIBL

PERMISSIONS http://www.sciencemag.org/help/reprints-and-permissions

Use of this article is subject to the Terms of Service